Atomistic simulations of the wetting behavior of nanodroplets of water on homogeneous and phase separated self-assembled monolayers†

Jonathan D. Halverson,*[a] Charles Maldarelli,[b] Alexander Couzis[c] and Joel Koplik[d]

Received 20th October 2009, Accepted 16th December 2009
First published as an Advance Article on the web 28th January 2010
DOI: 10.1039/b921840h

The wetting behavior of water nanodroplets on homogeneous and phase separated self-assembled monolayers (SAMs) composed of $CH_3(CH_2)_{10}SH$ and $HOCH_2(CH_2)_{10}SH$ on Au(111) was studied using molecular dynamics simulation. A simple model is introduced for the SAM where only the top eight or ten atomic layers are considered. For the homogeneous monolayers the CH_3– and $HOCH_2$–terminated chains are uniformly mixed. With χ_p denoting the mole fraction of $HOCH_2$-terminated chains, we report the equilibrium contact angles of water droplets composed of 4000 molecules on homogeneous monolayers for $\chi_p = 0$, 0.25, 0.5, 0.75, and 1. Good agreement is seen between the simulation results and experimental data for millimetre-size drops. For $\chi_p = 0.5$, the contact angle and base diameter of the droplet are found to be $51.9 \pm 1.3°$ and 10.2 ± 0.2 nm, respectively. Large deviations from the Cassie model are observed while the Israelachvili-Gee equation gives a better prediction. For the monolayers with $\chi_p = 0$ and 0.25, we estimate the line tension through the drop-size dependence of the contact angle and find good agreement with theoretical predictions. For the phase separated monolayers, the $HOCH_2$-terminated chains are organized into randomly-located circular domains which are embedded in a background matrix of CH_3-terminated chains. With $\chi_p = 0.5$, we consider two domain sizes with the diameters of the small and large domains being 1 and 2 nm. The water contact angle is found to be 63.1° for the monolayer with small domains and 68.1° for the monolayer with large domains. The results for the homogeneous and phase separated monolayers with $\chi_p = 0.5$ indicate that the nanoscale wetting behavior of the SAM is sensitive to its nanostructure.

1 Introduction

Self-assembled monolayers (SAMs) of alkanethiols on noble metals have received much attention in recent years because they are simple to prepare and provide well-ordered, dense monolayers.[1] SAMs have been used in a broad range of areas including biocompatibility,[2,3] molecular electronics,[4,5] corrosion,[6] and wettability.[7–12] The wettability of a SAM may be tuned by the choice of terminal functional group or by the mixing ratio of multi-component SAMs. Given the consistency of the monolayer at full coverage, a pure liquid drop on a single-component SAM is expected to follow the Young-Dupré equation:

$$\gamma_{SV} - \gamma_{SL} = \gamma \cos \theta, \quad (1)$$

where γ is the liquid–vapor tension, γ_{SL} is the solid–liquid tension, γ_{SV} is the solid–vapor tension, and θ is the equilibrium contact angle.

Many applications require self-assembled monolayers to be patterned at small scales. Microcontact printing,[13] photolithography[14,15] and other methods have been shown to pattern SAMs at the microscale. To chemically pattern surfaces at the nanoscale, techniques such as nanoshaving,[16,17] electrochemical etching, or dipped-pen nanolithography[18] may be used. These methods rely on a scanning probe microscope (SPM) and while the designs they produce are intricate, they are limited to square-micron sized planar areas. SAMs may also be patterned at the nanoscale by the coadsorption approach where mixed monolayers spontaneously phase separate. Typically, this produces single-component domains of nanometre size. A second approach is sequential adsorption where one component is allowed to form islands on the substrate before a second component is added to serve as the background matrix. The SPM approaches offer far more control of the pattern in comparison to the latter two techniques. However, mixed and sequential adsorption are easier to employ and may be applied to curved surfaces such as those of micro[19] and nanoparticles.[20] They may also be applied to surfaces of macroscopic dimensions.

The majority of coadsorption studies have used ethanol as the solvent and Au(111) as the metal surface. In an early study of mixtures of methyl- and hydroxyl-terminated alkanethiols of similar chain length, Whitesides and coworkers[7] concluded that the chains were not necessarily randomly dispersed and that

[a]*Department of Chemical Engineering, City College of New York, New York, NY, 10031, USA. E-mail: halverson@mpip-mainz.mpg.de*
[b]*Department of Chemical Engineering and Levich Institute, City College of New York, New York, NY, 10031, USA*
[c]*Department of Chemical Engineering, City College of New York, New York, NY, 10031, USA*
[d]*Department of Physics and Levich Institute, City College of New York, New York, NY, 10031, USA*

† Electronic supplementary information (ESI) available: oxygen-oxygen radial distribution functions for three monolayers with different degrees of phase-separation and $\chi_p = 0.5$ (Fig. S1); wet and dry heights of the homogeneous monolayers (Table S1); transverse components of the center-of-mass position of the droplet shown for all time on a homogeneous monolayer (Fig. S2). See DOI: 10.1039/b921840h

single-component domains may be present at tens of angstroms in size. Using infrared reflection-absorption spectroscopy (IRAS), Bertilsson and Liedberg[21] concluded that the chains in mixed monolayers of hexadecanethiol and 16-mercapto-1-hexadecanol showed complete mixing when χ_p was less than one half. Stranick *et al.*[22] using scanning tunneling microscopy (STM) showed that mixed monolayers of $CH_3(CH_2)_{15}SH$ and $CH_3O_2C(CH_2)_{15}SH$ on Au(111) formed nanometre scale molecular domains. The two alkanethiols in this case have similar chain length and are weakly interacting (*i.e.*, they do not hydrogen bond with one another). The size of the domains was reported to be 2–10 nm. Nanoscale phase-segregation was later confirmed for mixtures of $HOCH_2(CH_2)_{15}SH$ and $CH_3(CH_2)_{15}SH$ and ruled out for $NCCH_2(CH_2)_{15}SH$ and $HOCH_2(CH_2)_{15}SH$.[23]

The atomic force microscopy (AFM) studies of Tamada *et al.*[24] also showed single-component domains of size 10–20 nm for a specific range of mixing ratios of 1-butanethiol and 1-octadecanethiol. Hayes *et al.*[25] used AFM and lateral force microscopy to investigate SAMs composed of $CH_3(CH_2)_{17}SH$ and 4-aminothiophenol, which differ significantly in chain length and terminal group chemistry. The SAMs were shown to phase separate into domains of 10–100 nm in size. This system is an ideal candidate for phase segregation because of the disparate nature of the two chains. Mixtures of $HO_2C(CH_2)_2SH$ and $CH_3(CH_2)_{15}SH$ have been shown to phase separate.[26,27] Depending on the solution concentration for this system, the area of the domains was found to vary from tens to hundreds of square-nanometres. Monolayers formed from $HO_2C(CH_2)_{10}SH$ with either $CH_3(CH_2)_9SH$[28] or $CH_3(CH_2)_{10}SH$[27,29] have been shown to give homogeneous mixtures despite the difference in terminal group chemistry. STM studies by Lewis *et al.*[30] found phase separation for mixtures of $CH_3(CH_2)_9SH$ and two of the three amine-containing alkanethiols considered. An equimolar solution of 1-decanethiol and 3-mercapto-*N*-nonylpropionamide was found to phase separate with 1-decanethiol forming islands and the amine-containing alkanethiol serving as the background.

Salaita *et al.*[31] combined dip-pen nanolithography with a phase separating binary solution containing $HO_2C(CH_2)_{15}SH$ to achieve an enhanced degree of patterning resolution. Ternary systems[32] have also been shown to phase separate as well as binary systems on curved substrates.[20] Much less is known about nanoscale phase separation for SAMs composed of alkylsilanes, which are a class of materials that adsorb on hydroxylated surfaces and have structural properties similar to those of the alkanethiols.

Brewer and Leggett[33] have conducted chemical force microscopy (CFM) studies on pure and mixed monolayers of $CH_3(CH_2)_{11}SH$ and $HO(CH_2)_{11}SH$. For the pure monolayers the pull-off force measurements are found to follow a Gaussian distribution. However, the mixed monolayers give distributions that are broad and, for certain mixing ratios, have a bimodal appearance. Frictional force microscopy (FFM), which has a larger tip–sample contact area than CFM, suggested that the monolayers were uniformly mixed for all compositions. After comparing the estimated contact areas for CFM and FFM to previously reported island sizes for similar SAMs, the authors concluded that single-component domains with areas less than or equal to 15 nm^2 are present in the mixed monolayers. These results and those of Stranick *et al.*[23] and Bain *et al.*[7] are particularly important for the present work where nanoscale phase separation for mixtures of $CH_3(CH_2)_{10}SH$ and $HOCH_2(CH_2)_{10}SH$ on Au(111) is assumed.

A number of macroscale experimental studies have examined the effect of phase separation on the wetting behavior of SAMs. Imabayashi *et al.*[27] examined the water contact angle of homogeneous and artificially phase-separated monolayers of undecanethiol and 11-mercaptoundecanoic acid. The domain size for the phase separated monolayers was 5–20 nm. The water contact angle of millimetre-size drops was found to be the same for both monolayers over the entire range of compositions. The wetting data were shown to agree with the Cassie equation. The Cassie equation[34] is an empirical expression that relates the macroscopic contact angle of a pure fluid on an atomically-smooth, solid surface to the area fractions of the materials composing the surface:

$$\cos\theta = f_1 \cos\theta_1 + f_2 \cos\theta_2. \quad (2)$$

In eqn (2), f_i is the area fraction of component i and θ_i is the contact angle of the fluid on a surface of pure i. When the size of the domains approaches molecular dimensions the Israelachvili-Gee equation[35] should be used:

$$(1 + \cos\theta)^2 = f_1(1 + \cos\theta_1)^2 + f_2(1 + \cos\theta_2)^2. \quad (3)$$

Fig. 1 shows the behavior of water drops of different size on a heterogeneous substrate.

Molecular simulations using interaction potentials for real materials have proven successful in the study of wetting phenomena. Using molecular dynamics simulations, Hautman and Klein[36] showed that a droplet composed of as few as 90 molecules could be used to estimate the water contact angle of either methyl- or hydroxyl-terminated SAMs. The authors point out that such agreement is expected when the bulk region of the droplet is of sufficient size (*i.e.*, the height of the drop is greater than the sum of the liquid–vapor and solid–liquid interfacial thicknesses). Other simulation studies have sought to reproduce the equilibrium contact angles of real fluids on pure substrates.[37–40]

Recently, Lundgren *et al.*[39] examined the behavior of water nanodroplets on chemically and topologically heterogeneous substrates. They used the TIP-3P interaction potential for water while the substrate was modeled as a Lennard-Jones solid. For the flat, chemically heterogeneous substrates, when the ratio of the domain size to drop size was small, the Cassie model was found to hold over the entire composition range. However,

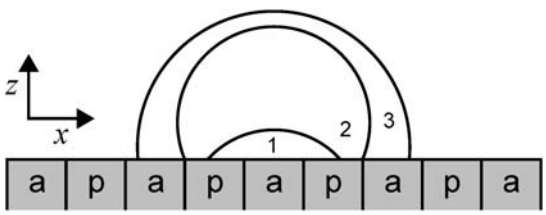

Fig. 1 The profiles of three water drops of different size are shown on a chemically heterogeneous substrate composed of polar (p) and apolar (a) regions.

significant deviations were seen as this ratio became large. This behavior was also found by studies using simple interaction potentials.

Mixtures of alkanethiols have been shown to form dense monolayers on gold. Many experimental studies have shown that for certain binary systems, due to a difference in chain length or terminal group chemistry, the two species will spontaneously phase separate to form a monolayer with nanometre-size single-component domains embedded in a background matrix of the second component. This has specifically been demonstrated for mixtures of CH_3- and $HOCH_2$-terminated chains of similar chain length. To understand how the nanoscale wetting behavior is affected by the degree of mixing of the chains, we have conducted molecular dynamics simulations to investigate this relationship (through the water contact angle) for homogeneous and phase-separated binary SAMs. While the mixing ratio for the homogeneous monolayers was varied over the entire composition range, for the inhomogeneous monolayers the degree of phase separation was only varied for the single choice of $\chi_p = 0.5$.

The results of previous studies concerning the wetting of solid substrates by nanodroplets of water have been extended by the current work. For the homogeneous SAMs, previous authors[36] have only investigated the water contact angle of either pure methyl- or hydroxyl-terminated monolayers. In the present work we vary the mixing ratio of the two chains which, in addition to providing new simulation data, also allows for the evaluation of the validity of the Cassie and Israelachvili-Gee equations. The line tension is calculated for our most hydrophobic monolayers. And while Lundgren *et al.*[39] considered the wetting of generic substrates, the present work considers homogeneous and phase separated SAMs with real interaction potentials which allows for the direct comparison with experimental data.

1.1 SAM model

The accepted structure of SAMs composed of alkanethiols on Au(111) has changed many times over the years[1,41,42] and is still being refined.[43] The monolayer was first thought to form a $(\sqrt{3} \times \sqrt{3})R30^\circ$ structure[44] with the sulfur atoms in the triple-fold hollow sites of the gold lattice. Infrared absorption studies by Nuzzo *et al.*[45] indicated a structure with two chains per unit cell. Evidence from low temperature helium diffraction experiments[46] and grazing incidence X-ray diffraction studies[47] suggested a $c(4 \times 2)$ superlattice. This structure was later confirmed by STM.[48–50]

Computer simulation has proven to be a useful tool for investigating the structural properties of self-assembled monolayers. Most SAM models are based on the early united-atom and all-atom models of Klein and coworkers.[51–54] These models and their derivatives have been used to elucidate the structural details of the $c(4 \times 2)$ superlattice[53,55–57] and to determine the effects of temperature,[52,58,59] chain length,[59–61] and lattice spacing[59,61] on the structure of the monolayer. Recently, Riposan and Liu, based on their STM results and the computer simulation results of Li *et al.*,[57] have proposed a structural model for undecanethiol on Au(111).[62] A modified version of this model is used for the present study.

The homogeneous and phase separated monolayers used in this work are composed of 50 chains in the x-direction and 58 chains in the y-direction. We adopt the model for Phase B of Riposan and Liu[62] where the monolayer forms a $(4\sqrt{3} \times 2\sqrt{3})R30^\circ$ lattice or $c(4 \times 2)$ superlattice. The sulfur atoms are located in the triple-hollow sites where they form a triangular lattice with nearest-neighbor spacing $a = 4.97$ Å. Each of the four chains per unit cell has the same tilt angle ($\theta = 30^\circ$) and direction of tilt ($\chi = 15^\circ$). The individual twist angles are different. Fig. 2 and 3 show the structural model used in our work.

The wetting properties of SAMs composed of alkanethiols become independent of chain length when the number of methylene groups in the chain becomes large. Specifically, this has

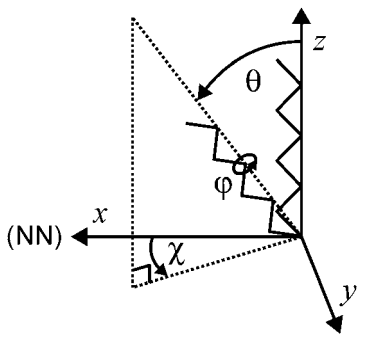

Fig. 2 The orientation of each chain in the monolayer is described by a tilt angle (θ), a direction of tilt (χ), and a twist angle about the molecular axis (φ). This diagram is shown for a methyl-terminated chain with its eight atomic units. The x-direction corresponds to a nearest-neighbor (NN) direction.

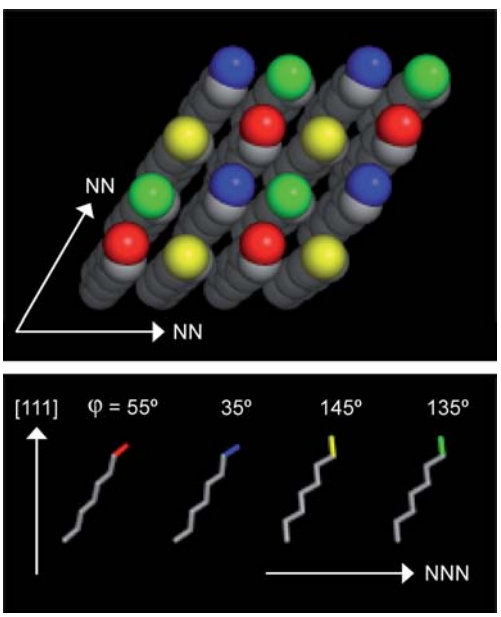

Fig. 3 The top image shows the top view of a region of a methyl-terminated monolayer. The twist angles are indicated by color in the bottom image. Monolayers with alcohol-terminated chains have the same structure. The next-nearest neighbor (NNN) direction corresponds to $\chi = 30^\circ$ in Fig. 2.

been shown for mixed monolayers of $CH_3(CH_2)_nSH$ and $HOCH_2(CH_2)_nSH$ for $n = 10$ and 18[7] and $CH_3(CH_2)_nSH$ and $HO_2C(CH_2)_nSH$ for $n = 10$ and 15.[7,63] To reduce computation time we therefore only consider the top eight or ten atomic layers of the monolayer (depending on the terminal group) and ignore the remaining methylene groups, sulfur atoms, and gold lattice. Methyl and methylene groups are treated as united atoms while the oxygen and hydrogen atoms of the hydroxyl group are treated atomically. This means that methyl-terminated chains are composed of eight atomic units or $-(CH_2)_7CH_3$ while hydroxyl-terminated chains are composed of ten or $-(CH_2)_7CH_2OH$. The positions of the bottom two atomic layers (or three for one simulation) of the monolayer are fixed throughout the simulation. This keeps the self-assembled monolayer in place and helps to impose the proper structure on the chains. A similar approach has been utilized for $HO(CH_2)_{11}SH/Au$[12]. Because these reduced monolayer models are based on full monolayers under specific conditions they are less general and caution must be exercised in extrapolating them to systems under different conditions.

While the model of Riposan and Liu[62] was proposed for 1-undecanethiol, evidence exists to suggest that it also applies to 11-mercapto-1-undecanol. Dannenberger *et al.*[64] have shown that the overall structure of pure methyl- and hydroxyl-terminated SAMs are similar for chains of the same length. For instance, they find $CH_3(CH_2)_{21}SH$ and $HOCH_2(CH_2)_{21}SH$ on Au(111) to have a thickness of 25.4 and 25.9 Å, respectively. When the number of methylene groups is reduced by six both monolayers give a height of 18.9 Å. The tilt angles for these monolayers as determined by XPS and near edge X-ray absorption fine structure spectroscopy (NEXAFS) are also very similar. Sprik *et al.* conducted molecular dynamics simulations to investigate the structure of pure SAMs with OH and NH_2 terminal groups.[54] Their results show a similar overall structure when compared to SAMs with methyl termination.

The starting point for the construction of the mixed monolayers was a methyl-terminated monolayer with each chain *trans*-extended. Alcohol-terminated chains were introduced by randomly selecting a methyl-terminated chain and replacing its CH_3 group with a $HOCH_2$ group. The alcohol-terminated chain took on the values of θ, χ, and φ of the methyl-terminated chain. This process was repeated until the desired value of χ_p was achieved. The phase separated monolayers were constructed in a similar manner. A single chain was selected at random. If this chain and the six closest chains to it (or eighteen in the case of the large domains) were methyl-terminated then a domain was created by changing the termination of each chain to a $HOCH_2$ group.

The domain sizes of 1 and 2 nm in the present work are within the size ranges reported by experimental studies. For CH_2OH/CH_3 systems, Bain *et al.*[7] put the upper limit on the domain size as a few tens of angstroms. Stranick *et al.*[23] did not cite a numerical value but instead reported nanometre-scale domains. For OH/CH_3 systems, Brewer and Legget[33] argue for single-component domains with areas less than or equal to 15 nm^2 (or 3.9 nm in length). Less is known about the distribution of domains and which of the two components form the islands. In creating our phase segregated monolayers we have assumed that the domains are randomly distributed and occupied by alcohol-terminated chains.

2 Simulation methodology

The wetting behavior of water droplets composed of 4000 molecules was examined on binary self-assembled monolayers. A droplet was constructed by extracting a hemispherical cluster from a large simple cubic lattice of randomly-orientated water molecules arranged at ambient liquid density. The droplet was placed in the vicinity of the monolayer. The chains in the monolayer were initialized with $\theta = 30°$, $\chi = 15°$, and the twist angles indicated in Fig. 3. Conjugate gradient energy minimization was performed for 10 000 steps.

The molecular dynamics (MD) simulations[65] were carried out at constant number of molecules, system volume, and temperature using NAMD.[66] The temperature was maintained at 298.15 K by applying a Langevin thermostat, with a damping coefficient of 0.5 ps^{-1}, to non-hydrogen atoms. The Verlet method was used to perform the numerical integration of the equations of motion for the monolayer while SETTLE[67] was used for water. All bond lengths in the monolayer were kept fixed using SHAKE.[68] A timestep of 1 fs was used. The SPC/E interaction potential[69] was used for water while the OPLS-UA force field[70,71] was used for

Table 1 Force field for the MD simulations

Bond	Length/Å		
O–H[a]	1.000		
O–H	0.945		
CH_2–O	1.430		
CH_2–CH_2	1.530		
CH_2–CH_3	1.530		
Valence	k_θ	θ_0/°	
H–O–H[a]	—	109.47	
H–O–CH_2	110.02	108.5	
O–CH_2–CH_2	100.09	108.0	
CH_2–CH_2–CH_2	124.20	112.0	
CH_2–CH_2–CH_3	124.20	112.0	

The valence potential energy is given by $U = \frac{k_\theta}{2}(\theta - \theta_0)^2$.
k_ϕ is given in units of kcal mol^{-1} rad^{-2}.

Dihedral	V_1	V_2	V_3
H–O–CH_2–CH_2	0.834	–0.116	0.747
O–CH_2–CH_2–CH_2	0.702	–0.212	3.060
CH_2–CH_2–CH_2–CH_2	1.411	–0.271	3.145
CH_2–CH_2–CH_2–CH_3	1.411	–0.271	3.145

The dihedral potential energy is given by

$$U = \tfrac{V_1}{2}(1 + \cos\phi) + \tfrac{V_2}{2}(1 - \cos 2\phi) + \tfrac{V_3}{2}(1 + \cos 3\phi).$$

V_i are given in units of kcal mol^{-1}.

Nonbonded i–i	σ_{ii} (Å)	ε_{ii}	q_i (e)
H–H[a]	0.0	0.0	0.4238
O–O[a]	3.166	650.2	–0.8476
H–H	0.0	0.0	0.265
O–O	3.070	711.8	–0.700
CH_2–CH_2[b]	3.905	493.9	0.435
CH_2–CH_2[b]	3.905	493.9	0.0
CH_3–CH_3	3.905	732.5	0.0

The Lennard-Jones potential energy is given by
$U = 4\varepsilon_{ij}[(\sigma_{ij}/r_{ij})^{12} - (\sigma_{ij}/r_{ij})^6]$.
ε_{ij} are given in units of J mol^{-1}.

[a] These parameters apply to SPC/E water while all others apply to the binary SAM. [b] A CH_2 united atom is neutral except when directly bonded to an alcohol group where it has a partial charge of 0.435e. The OPLS combining rules are

$$\sigma_{ij} = \sqrt{\sigma_{ii}\sigma_{jj}}$$

and

$$\varepsilon_{ij} = \sqrt{\varepsilon_{ii}\varepsilon_{jj}}.$$

the monolayer (see Table 1). The OPLS combining rules were used for water-monolayer interactions. The interactions between atoms in the same monolayer chain separated by three or fewer bonds were excluded. Short-range interactions were cutoff at 12 Å with a switching function applied for separations greater than 10 Å. The dimensions of the simulation cell were $L_x = 258.50$ Å, $L_y = 249.64$ Å, and $L_z = 250.00$ Å. Periodic boundary conditions in three dimensions were used. The particle-mesh Ewald (PME) technique[72,73] was used to account for long-range interactions with the smallest number of grid points per direction being 0.92 Å^{-1}. The simulations were run on DataStar at the San Diego Supercomputer Center.

One run was carried out for each of the five homogeneous monolayers. Because the spreading rate varies with monolayer composition the total simulation time was different for each run with the $\chi_p = 0$ case needing only 4 ns and the $\chi_p = 1$ case requiring 13 ns. For the phase separated monolayers, seven runs of 4 ns each were carried out for both the 1 and 2 nm domain cases for the only choice of $\chi_p = 0.5$.

Several checks were performed using a homogeneous monolayer with $\chi_p = 0.5$ to ensure that the chosen simulation parameters were not introducing artifacts. In two separate simulations the transverse area and height of the simulation cell were doubled keeping the number of grid points per direction constant in the PME calculation. The contact angles and wetting dynamics were found to be very similar to the original case suggesting that image droplets were not influencing the results. The effect of different droplet shapes at initialization was also studied. With each case having the same number of total water molecules, we considered a rectangular drop, a spherical drop, and two spherical drops separated by a few angstroms. In all cases the average contact angle was found to be within one degree of θ for the reference case. A similar result for water on graphite was found by Werder *et al.*[40] The fact that the contact angle is independent of the initial shape of the drop is not surprising because thermal fluctuations at this scale are sufficiently large to quickly drive the system out of metastable states. Because of this, for the monolayers considered in this work the contact angles we report are the equilibrium values.

3 Results and discussion

3.1 SAM Structural properties

Simulations of the monolayer in the absence of water were conducted to determine its structural properties. Two different choices of χ_p were considered. Each simulation was performed for 400 ps with average values computed over the final 200 ps.

The atomic density profiles normal to the surface are shown in Fig. 4 for $\chi_p = 0$ and 0.5. In Fig. 4a, the methyl and methylene distributions have been combined into a single curve. The atomic density of these groups is seen to vary sharply with position indicating that the atoms are largely constrained to equilibrium sites. The distribution of carbon-containing groups is very similar for the two monolayers (Fig. 4a,b). This suggests that the addition of $HOCH_2$ groups to half of the chains has little impact on the underlying structure. For $\chi_p = 0.5$, the oxygen and hydrogen atoms are found to be broadly distributed in

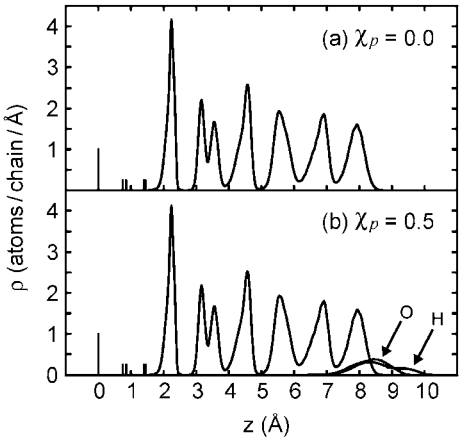

Fig. 4 Atomic density profiles normal to the surface for two choices of χ_p.

comparison to any methylene group in the chain. This behavior is due to lateral hydrogen bonding between adjacent alcohol-terminated chains.

With the bottom two atoms of each chain being fixed, the four different twist angles lead to five planes where the methylene density is constant. These planes correspond to the vertical lines in Fig. 4. There are four times as many atoms in the $z = 0$ plane as in the planes at $z = 0.75$, 0.85, 1.40, and 1.45 Å. While the atomic densities at each of these locations are mathematically infinite, in Fig. 4 they have been drawn with a magnitude equal to the contribution they make to the integral $\int_{-\infty}^{\infty} \rho_C(z)\, dz$, where $\rho_C(z)$ is the density of carbon-containing groups at z. That is, the distribution at $z = 0$ contributes 1 atom/chain while the others each contribution 1/4.

In the model used here CH_3- and $HOCH_2$-terminated chains have five and seven dihedral angles, respectively. The percentage of *gauche* defects as a function of dihedral angle number for the two monolayers is shown in Fig. 5. For both monolayers there are few *gauche* defects for dihedral angles 1 through 5. For $\chi_p = 0.5$, angles 6 and 7 show a high percentage of defects. This is attributed to lateral hydrogen bonding and is consistent with experimental findings.[1]

The distribution function for the chain tilt angle is shown in Fig. 6. The tilt angle is the angle between a unit normal surface vector, $\boldsymbol{n}$, and the vector formed by the average position of the

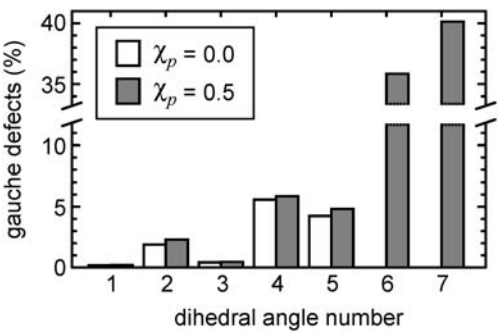

Fig. 5 Percentage of *gauche* defects as a function of dihedral angle number for two choices of χ_p. The numbering scheme begins with angle 1 which involves the two fixed atoms. Note that the ordinate is interrupted.

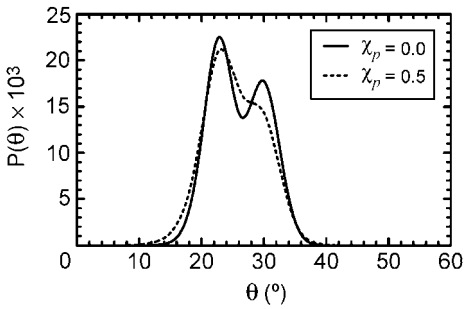

Fig. 6 Probability distribution function for the tilt angle for two choices of χ_p.

fixed atoms and the average position of the free atoms per chain, r. The model suggested by Riposan and Liu[62] has a tilt angle of 30° for all chains. Our simulations for $\chi_p = 0$ and 0.5 give average tilt angles of 26.0 and 25.4°, respectively. The double peak for the methyl-terminated monolayer is due to the rigidity of the bottom atomic layers and the two pairs of similar twist angles. When $HOCH_2$ groups are present, as with the $\chi_p = 0.5$ case, hydrogen bonding disrupts the tilt angle distribution in such a way that the two peaks are replaced by a single peak with a shoulder.

Fig. 7 shows the distribution function for the direction of tilt. The angle χ is formed by a unit vector pointing in the x-direction (or NN direction) and $\langle r_x, r_y, 0\rangle$. At initialization, the tilt direction of each chain is set to $\chi = 15°$ (or the NNNN direction) as prescribed by the model of Riposan and Liu.[62] The monolayer was found to relax during the early stages of the simulation. The equilibrium distributions for both monolayers are found to be centered about $\chi = 29°$ or the NNN direction. This shift is allowed to take place because only the bottom two atomic layers are fixed. An additional simulation was performed for the $\chi_p = 0$ monolayer with the bottom three atomic layers kept fixed. This resulted in a tilt angle distribution that was very similar to the original case. With three fixed atoms the chain backbone becomes far more inflexible, which is due to the strong preference for the all-*trans* conformation. The distribution of the direction of tilt was found to be centered about $\chi = 21°$, which is closer to the target value of 15°. As the number of fixed atoms per chain increases the model becomes less realistic, but given the improvement in the structure this choice would also be reasonable.

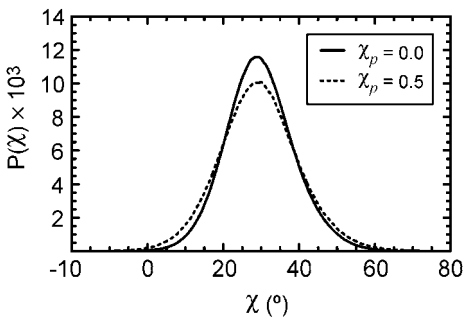

Fig. 7 Probability distribution function for the direction of tilt for two choices of χ_p. Nearest-neighbor directions correspond to $\chi = 0$ and 60° while the next-nearest neighbor direction corresponds to $\chi = 30°$.

We have also conducted simulations to investigate the effect of the number of fixed atoms per chain on the water contact angle. For these simulations the monolayer was composed of $-(CH_2)_7CH_3$ and $-(CH_2)_6OH$ with the chains arranged in the $(\sqrt{3} \times \sqrt{3})R30°$ structure. For $\chi_p = 0.5$, when the number of fixed atoms per chain was 8, 6, and 2, θ was found to be 83.2, 80.1, and 77.6°, respectively. The last two values are within one standard deviation of each other indicating convergence. Because hydrogen bonding is highly directional, as the number of fixed atoms per chain increases the average number of hydrogen bonds formed between the monolayer and the droplet decreases. This explains why the contact angle increases with the number of fixed atoms per chain.

3.2 Homogeneous monolayers

The wetting behavior of droplets of water composed of 4000 molecules was examined on uniformly-mixed SAMs. Monolayers with $\chi_p = 0$, 0.25, 0.5, 0.75, and 1 were considered. At $t = 0$, the hemispherical water droplet was placed in the vicinity of the substrate with its center-of-mass aligned with the origin in the xy-plane. The system was then evolved in time according the MD method.

The normal component of the center-of-mass position of the droplet *versus* time is shown in Fig. 8 for five choices of χ_p. As χ_p increases, the surface energy of the monolayer increases and the droplet is found to spread more. For $\chi_p = 0$ or the methyl-terminated monolayer, z_{CM} is seen to increase during the first 200 ps of the simulation and then fluctuate about its equilibrium value of 30.8 Å. Over the last 1.5 ns of the simulation the instantaneous value of z_{CM} never deviates from the average value by more than ± 2 Å. For the $\chi_p \geq 0.75$ cases, the center-of-mass position is seen to decrease with time before fluctuating about an equilibrium value. Once equilibrium has been established deviations from the average value of z_{CM} are less than ± 1 Å for each of these cases. The simulation with $\chi_p = 1$ was run for 13 ns to ensure that spreading had stopped.

Side views of the final configurations for $\chi_p = 0$, 0.5, and 1 are shown in Fig. 9. The water droplet on the CH_3-terminated monolayer in Fig. 9a is seen to have a contact angle larger than 90°. As χ_p increases the droplet spreads more. Fig. 9c shows that the droplet on the $HOCH_2$-terminated monolayer has spread to a thickness of a few molecules. No bulk region is present in this case. The tilt of the chains is clearly seen as well as *gauche* defects

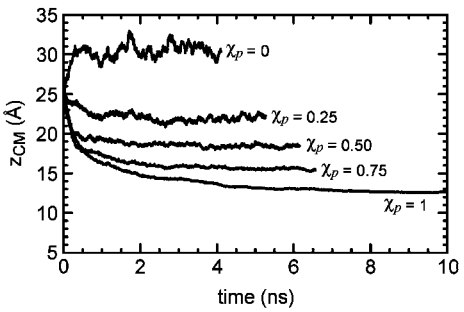

Fig. 8 The normal component of the center-of-mass position of a water droplet on a homogeneous SAM as a function of time for different values of χ_p. The bottom layer of fixed atoms is located at $z = 0$.

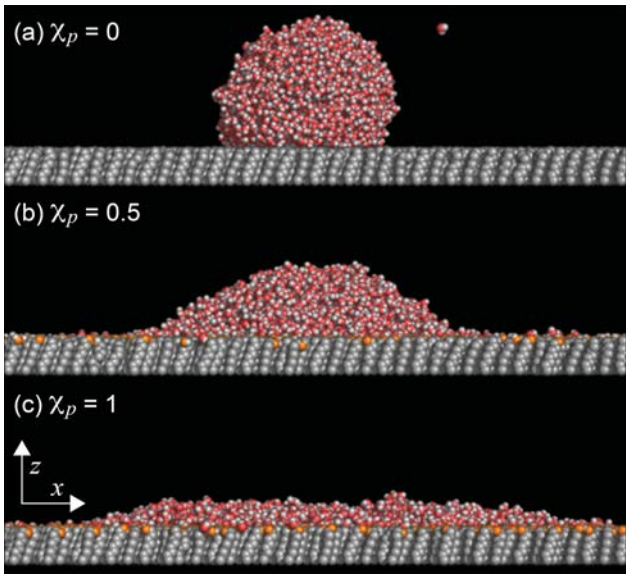

Fig. 9 Side views of the final configurations from three different simulations of a water droplet composed of 4000 molecules on a homogeneous SAM with (a) $\chi_p = 0$, (b) $\chi_p = 0.5$, and (c) $\chi_p = 1$. The width of the simulation cell is roughly 50 Å larger than shown. The water molecules are shown with oxygen colored red and hydrogen in white, while the substrate is shown with methyl and methylene groups as gray, oxygen as orange, and hydrogen as white.

near the top of each monolayer. The top view of the $\chi_p = 0.5$ case is shown in Fig. 10. Occasionally, one or two water molecules will detach from the droplet and act as a vapor. An example of this is seen in Fig. 9a. This behavior has been reported by other authors for similar systems[36,39] and is expected based on the saturation properties of water.

The procedure of de Ruijter *et al.*[74] with the parameters of Werder *et al.*[40] were used to determine the equilibrium shape of each droplet. The best-fit circle, liquid–vapor boundary profile data points, and tangent line at the droplet edge are shown in Fig. 11 for the $\chi_p = 0.5$ case. The equilibrium contact angle, height, base radius, and average value of z_{CM} for each droplet on the homogeneous SAMs are given in Table 2. The

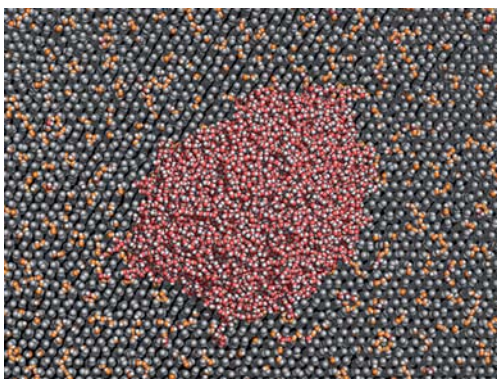

Fig. 10 Top view of the final configuration of a water droplet composed of 4000 molecules on a homogeneous SAM with $\chi_p = 0.5$. The base area of the simulation cell is roughly twice as large as that shown. Same color scheme as Fig. 9.

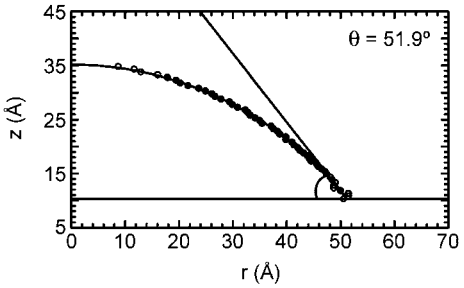

Fig. 11 The best-fit circle and liquid–vapor boundary profile data points are shown for a water nanodroplet on a homogeneous SAM with $\chi_p = 0.5$. The tangent line at the droplet edge is also shown. The wet height of the monolayer is indicated by the horizontal line. The bottom layer of fixed atoms is located at $z = 0$. The open circles near apex and edge of the droplet were ignored when the best-fit circle was determined. For the fit we find $E = 0.28$ Å.

Table 2 Wetting behavior of a nanodroplet of water on a homogeneous SAM for different choices of χ_p. The microscopic contact angle is θ, the droplet height and base radius are h and r_B, the z-component of the average center-of-mass position is z_{CM}, and E is the root-mean-square error of the best-fit circle to the boundary profile data. h, r_B, z_{CM}, and E are in units of Å

χ_p	θ/°	h	r_B	z_{CM}	E
0.00	121.9	49.1	27.3	30.8	0.20
0.25	75.9	33.4	42.8	22.1	0.27
0.50	51.9	24.9	51.2	18.5	0.28
0.75	30.5	16.9	62.2	15.6	0.32
1.00	11.6	8.8	86.1	12.7	0.66

root-mean-square error, E, is used as a measure of the fit between the best-fit circle and the time-averaged liquid–vapor boundary profile. The value of E is fairly constant with the exception of the $\chi_p = 1$ case. For this case, since the shape of the droplet is not that of a spherical cap the contact angle and other properties can only be taken as estimates.

In Fig. 12, the simulation results for the cosine of the water contact angle are compared with the experimental data of Bain *et al.*[7] (Fig. 4 of the original work). Good agreement is seen between the two data sets. Cassie's law and the Israelachvili-Gee equation are shown based on the simulation results and the experimental data. Poor agreement is seen between the Cassie equation and the actual measurements. For instance, if the Cassie equation were based on the simulation results it would predict a contact angle of 77.0° for $\chi_p = 0.5$ while the simulation value is 51.9°. The Israelachvili-Gee equation is seen to be an improvement over the Cassie prediction.

In Fig. 12, we have compared macroscopic contact angles measured for millimetre-size drops with microscopic values measured for nanometre-size drops. For nanometre-size drops the line tension may influence the measured contact angle[75–77]:

$$\cos\theta = \cos\theta_\infty - \frac{\tau}{\gamma}\frac{1}{r_B}, \quad (4)$$

where θ_∞ is the macroscopic contact angle and τ is the line tension. Within the context of our simulations, the exact contribution of the line tension can be obtained by plotting the

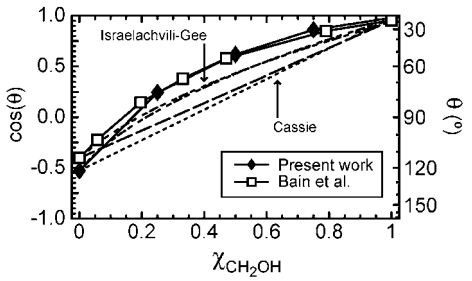

Fig. 12 Comparison of the wetting data between simulation and experiment. Error bars for the simulation data points are smaller than the size of the symbols.

simulated contact angle against the inverse of the drop radius and extrapolating to infinite radii in accordance with eqn (4). However, construction of these plots is difficult because to accurately measure the contact angle the simulation requires large droplets where the interfacial regions are small compared to the bulk region and this is especially difficult for small contact angles ($\chi_p > 0.5$). In constructing these plots, we have found for $\chi_p = 0$ and 0.25, which have large contact angles, line tensions of the order of 10^{-11} N are obtained, which are in agreement with theoretical predictions[76] and demonstrate a difference in contact angles of approximately seven degrees for $\chi_p = 0$ (128.5 and 121.9) with a negative line tension and fifteen degrees for $\chi_p = 0.25$ (58.0 and 75.9) and a positive line tension.

The height of the monolayer was computed using the approach of Hautman and Klein.[36] The height is taken as the average z-coordinate of the methyl and oxygen atomic centers plus terms to account for the size of the atoms. The wet height is computed using only chains that are beneath the droplet whereas the dry height is based on chains away from the droplet. All contact angles were calculated using the wet height. Further details of the monolayer height as well as the oxygen-oxygen radial distribution function may be found in the ESI.†

The SPC/E model[69] does better than most simple models at reproducing the bulk and interfacial properties of water.[78,79] However, its larger negative value for the potential energy of bulk water implies a larger water–water interaction strength. Because of this, it predicts higher contact angles in comparison to the other models. For instance, Werder *et al.*[40] found for a water droplet on a graphite-like substrate that the SPC/E and TIP-3P models with the same water–substrate interaction gave 65.4 and 48.0°, respectively. It should be noted from this that if another model were used it would be expected to give smaller values of θ.

3.3 Phase separated monolayers

For the study of phase separated monolayers the overall composition was fixed at $\chi_p = 0.5$. The $HOCH_2$-terminated chains were arranged into circular, single-component domains while the CH_3-terminated chains served as the background. Two domain sizes were considered. The 1 and 2 nm domains were composed of 7 and 19 chains, respectively. With reference to the structure at initialization, a 1 nm domain consists of a central chain and its six nearest neighbors at $r = a = 4.97$ Å. A 2 nm domain is a 1 nm domain with the addition of six next-nearest neighbor chains at $r = \sqrt{3}a \approx 8.61$ Å and six chains at $r = 2a = 9.94$ Å.

The same simulation protocol was followed for the phase separated monolayers as for the homogeneous cases. However, because the substrate is now heterogeneous seven runs were carried out for both the 1 and 2 nm domain cases to ensure that the results were not biased by a droplet spending a disproportionate amount of time in a local free energy minima. The locations of the domains were randomly assigned for each of the seven runs. Each simulation was performed for 4 ns with average values computed over the last 1.5 ns.

A representative snapshot from one of the runs with small domains is shown in Fig. 13. It can be seen that the droplet has an instantaneous shape that deviates from that of a spherical cap. This comes about by the droplet contorting its contact line in an attempt to cover hydrophilic domains while avoiding the hydrophobic background. Because of this, the droplet is mostly surrounded by methyl-terminated chains. In Fig. 13, the more isolated domains are seen to form ring-like hydrogen-bonding structures while adjacent domains form linear hydrogen-bonding structures.

The time-averaged droplet shapes for each of the seven wetting simulations for the phase separated monolayer with 1 nm domains are shown in Table 3. The average contact angle is 63.6°. The values of E indicate that the boundary profile data points are fit by a circle quite well. This emphasizes the notion that while droplet snapshots (*e.g.*, Fig. 13) may show large deviations from the spherical cap shape, when time averaged they indeed follow the expected form. The water contact angle for the phase separated monolayer with 1 nm domains was also computed by forming a single boundary profile using all of the configurations over the last 1.5 ns of each of the seven runs. When this was done the contact angle was found to be 63.5° with $E = 0.158$ Å. This result for θ is very similar to that of the previous approach. The contact angle computed in this manner is shown in Fig. 14.

A representative snapshot from one of the runs with large domains is shown in Fig. 15. Once again the instantaneous droplet shape is found to deviate from a spherical cap. The droplet is found to be surrounded by methyl-terminated chains while on top of a number of hydrophilic domains. As with the 1 nm domains, the $HOCH_2$-terminated chains of the 2 nm

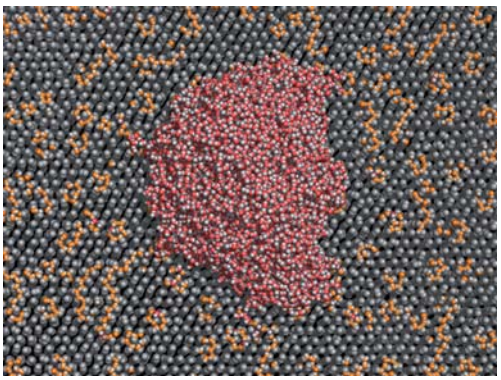

Fig. 13 Same as Fig. 10 except for a phase separated monolayer with 1 nm domains (Run 3 of Table 3).

Table 3 Same as Table 2 except for seven runs on a phase separated SAM with 1 nm domains and $\chi_p = 0.5$

Run	θ/°	h	r_B	z_{CM}	E
1	62.7	28.7	47.1	20.0	0.22
2	56.4	26.7	49.7	19.2	0.23
3	63.7	28.8	46.4	19.9	0.23
4	64.8	29.5	46.5	20.3	0.24
5	63.0	28.9	47.2	20.1	0.17
6	71.0	31.6	44.3	21.2	0.21
7	63.5	28.9	46.7	20.1	0.28

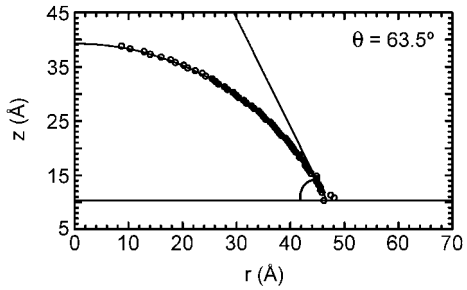

Fig. 14 Same as Fig. 11 except for a phase-separated SAM with 1 nm domains. For the fit we find $E = 0.158$ Å.

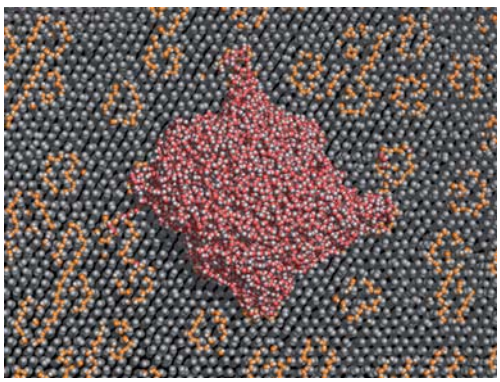

Fig. 15 Same as Fig. 10 except for a phase separated monolayer with 2 nm domains (Run 5 of Table 4).

domains are found to form hydrogen-bonding rings or linear chains depending on the spacing between domains.

The time-averaged droplet shapes for the monolayers with large domains are reported in Table 4. The average contact angle is found to be 66.5°. The average E is larger in this case than for the 1 nm domains. This indicates that the droplets are more distorted on the monolayer with large domains. When the configurations from all the production runs are used in forming a single boundary profile the contact angle is found to be 68.1° with $E = 0.163$ Å. The best-fit circle and boundary profile data points for the latter approach are shown in Fig. 16. Note that the values of E for the phase separated monolayers are both lower than the value for the homogeneous monolayer with $\chi_p = 0.5$. While snapshots of droplets on the phase separated monolayers show highly distorted shapes, when sufficient averaging is performed (through multiple simulations) the time-averaged boundary profile is found to be circular.

Table 4 Same as Table 2 except for seven runs on a phase separated SAM with 2 nm domains and $\chi_p = 0.5$

Run	θ/°	h	r_B	z_{CM}	E
1	64.5	28.0	44.5	19.4	0.45
2	71.3	31.7	44.2	21.2	0.20
3	75.0	32.1	41.8	21.0	0.28
4	62.9	28.7	46.9	20.0	0.22
5	70.8	31.3	44.0	21.0	0.14
6	65.9	29.4	45.4	20.2	0.28
7	54.8	25.7	49.6	19.3	0.79

For the same overall composition of $\chi_p = 0.5$, the water drops on the phase separated monolayers are found to give higher contact angles than the homogeneous monolayer by 12 and 19° for the small and large domain cases, respectively. An explanation for this behavior has been offered by Lundgren *et al.*[39] With reference to Fig. 1, one can imagine slowly increasing the volume of drop 1 while monitoring its profile. At early times, as fluid is added the base area of the drop increases while the contact angle remains the same. This continues until the edges of the drop encounter the interface between the polar and apolar regions. At this point the edges of the drop become pinned. As more fluid is added the base area remains the same while the contact angle increases (drop 2). Eventually the area of the liquid–vapor interface becomes so large that the free energy of the system is minimized when the edges of the drop are located on the apolar area (drop 3). If the surface is ideal then this transition will be smooth.

Similar behavior is seen in the simulations where it is the volume of the drop that is constant and the size of the domains that is changing. Table 5 indicates that as the domain size increases, the contact angle increases until the domain size becomes larger than the droplet size. This initial increase in θ comes about by the droplet decreasing its base area in order to cover hydrophilic domains while avoiding the hydrophobic background. This decrease in base area is accompanied by an increase in both the liquid–vapor interfacial area and the contact angle. Just as the free energy of the system was minimized by higher contact angles for the droplets in Fig. 1, the same is found here. As the domain size becomes larger than the droplet size, the droplet simply moves to a hydrophilic domain where it assumes the contact angle that it would have were it on the pure surface.

Lundgren *et al.*[39] found similar behavior to that in Table 5 for water droplets on surfaces composed of two materials. With the

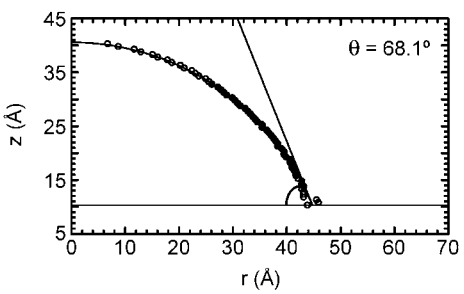

Fig. 16 Same as Fig. 11 except for a phase-separated SAM with 2 nm domains. For the fit we find $E = 0.163$ Å.

Table 5 A summary of the water contact angle for binary SAMs with the same overall composition but different degrees of mixing of the chains

χ_p	Nanostructure	θ/°
0.5	homogeneous	51.9
0.5	1 nm domains	63.5
0.5	2 nm domains	68.1
0.5	very large domains[a]	11.6

[a] When the domain size is much larger than the droplet size, the droplet is assumed to reside entirely on a hydrophilic domain.

area fractions of the two materials being equal, the water contact angle was found to initially increase with the ratio of domain size to droplet size and then decrease when this ratio became large. This was found in all cases for square array patterns as well as stripes (Fig. 3 and 6 of Lundgren *et al.*[39]).

4 Conclusions

Molecular dynamics simulations were conducted to investigate the wetting behavior of nanodroplets of water on binary self-assembled monolayers. The model introduced for the monolayer was found to give better agreement with experimental results when the bottom three atoms of the chains were kept fixed instead of only two. For the homogeneous monolayers the water contact angle was found to agree with the experimental data for all compositions. For the phase separated monolayers with an equimolar composition of CH_3- and $HOCH_2$-terminated chains, the water contact angle was found to depend of the domain size with the 1 and 2 nm domains yielding values of 63.5 and 68.1°, respectively. In both cases, θ was found to be larger than that for the homogeneous monolayer at the same overall composition suggesting that the wetting behavior is influenced by the degree of mixing of the chains.

The dependence of the contact angle on the domain size of the phase separated monolayers has important consequences for emerging technologies like nanofluidic[80] and lab-on-a-chip devices where precise knowledge of droplet behavior is needed. In these systems, droplets must be reliably controlled from one stage to the next and in order for this to be achieved the detailed interfacial behavior must be understood. Self-assembled monolayers will continue to be a common choice for these systems and, as demonstrated by experiment, when the surface energy is tuned by the mixed adsorption approach, phase separation is a reality.

Acknowledgements

This work was funded by a NSF IGERT Graduate Research Fellowship in Multiscale Phenomena of Soft Materials, and it was supported in part by the National Science Foundation through a large resource allocation (LRAC) on DataStar at the San Diego Supercomputer Center.

References

1 F. Schreiber, *Prog. Surf. Sci.*, 2000, **65**, 151.
2 K. L. Prime and G. M. Whitesides, *J. Am. Chem. Soc.*, 1993, **115**, 10714.
3 P. A. DiMilla, J. P. Folkers, H. A. Biebuyck, R. Härter, G. P. López and G. M. Whitesides, *J. Am. Chem. Soc.*, 1994, **116**, 2225.
4 C. Boulas, J. V. Davidovits, F. Rondelez and D. Vuillaume, *Microelectron. Eng.*, 1995, **28**, 217.
5 Y. Xia, X.-M. Zhao and G. M. Whitesides, *Microelectron. Eng.*, 1996, **32**, 255.
6 G. K. Jennings and P. E. Laibinis, *J. Am. Chem. Soc.*, 1997, **119**, 5208.
7 C. D. Bain, J. Evall and G. M. Whitesides, *J. Am. Chem. Soc.*, 1989, **111**, 7155.
8 C. D. Bain and G. M. Whitesides, *J. Am. Chem. Soc.*, 1989, **111**, 7164.
9 C. D. Bain, H. A. Biebuyck and G. M. Whitesides, *Langmuir*, 1989, **5**, 723.
10 J. P. Folkers, P. E. Laibinis and G. M. Whitesides, *Langmuir*, 1992, **8**, 1330.
11 P. Laibinis, R. Nuzzo and G. Whitesides, *J. Phys. Chem.*, 1992, **96**, 5097.
12 A. U. S. D. Evans, Y. Shnidman, R. Sharma and J. E. Eilers, *Adv. Colloid Interface Sci.*, 1992, **39**, 103.
13 J. L. Wilbur, A. Kumar, H. A. Biebuyck, E. Kim and G. M. Whitesides, *Nanotechnology*, 1996, **7**, 452.
14 E. W. Wollman, D. Kang, C. D. Frisbie, I. M. Lorkovic and M. S. Wrighton, *J. Am. Chem. Soc.*, 1994, **116**, 4395.
15 J. Y. Huang, D. A. Dahlgren and J. C. Hemminger, *Langmuir*, 1994, **10**, 626.
16 T. A. Jung, A. Moser, H. J. Hug, D. Brodbeck, R. Hofer, H. R. Hidber and U. D. Schwartzm, *Ultramicroscopy*, 1992, **42–44**, 1446.
17 X.-D. Xiao, G.-Y. Liu, D. H. Charych and M. Salmeron, *Langmuir*, 1995, **11**, 1600.
18 R. D. Piner, J. Zhu, F. Xu, S. Hong and C. A. Mirkin, *Science*, 1999, **283**, 661.
19 M. Preuss and H.-J. Butt, *J. Colloid Interface Sci.*, 1998, **208**, 468.
20 A. M. Jackson, J. W. Myerson and F. Stellacci, *Nat. Mater.*, 2004, **3**, 330.
21 L. Bertilsson and B. Liedberg, *Langmuir*, 1993, **9**, 141.
22 S. J. Stranick, A. N. Parikh, Y.-T. Tao, D. L. Allara and P. S. Weiss, *J. Phys. Chem.*, 1994, **98**, 7636.
23 S. J. Stranick, S. V. Atre, A. N. Parikh, M. C. Wood, D. L. Allara, N. Winograd and P. S. Weiss, *Nanotechnology*, 1996, **7**, 438.
24 K. Tamada, M. Hara, H. Sasabe and W. Knoll, *Langmuir*, 1997, **13**, 1558.
25 W. A. Hayes, H. Kim, X. Yue, S. S. Perry and C. Shannon, *Langmuir*, 1997, **13**, 2511.
26 S.-I. Imabayashi, D. Hobara and T. Kakiuchi, *Langmuir*, 1997, **13**, 4502.
27 S. Imabayashi, N. Gon, T. Sasaki, D. Hobara and T. Kakiuchi, *Langmuir*, 1998, **14**, 2348.
28 S. Arnold, Z. Q. Feng, T. Kakiuchi, W. Knoll and K. Niki, *J. Electroanal. Chem.*, 1997, **438**, 91.
29 T. Kakiuchi, M. Iida, N. Gon, D. Hobara, S.-I. Imabayashi and K. Niki, *Langmuir*, 2001, **17**, 1599.
30 P. A. Lewis, R. K. Smith, K. F. Kelly, L. A. Bumm, S. M. Reed, R. S. Clegg, J. D. Gunderson, J. E. Hutchison and P. S. Weiss, *J. Phys. Chem. B*, 2001, **105**, 10630.
31 K. Salaita, A. Amarnath, D. Maspoch, T. B. Higgins and C. A. Mirkin, *J. Am. Chem. Soc.*, 2005, **127**, 11283.
32 P. H. Phong, V. V. Sokolov, N. Nishi, M. Yamamoto and T. Kakiuchi, *J. Electroanal. Chem.*, 2007, **600**, 35.
33 N. J. Brewer and G. J. Leggett, *Langmuir*, 2004, **20**, 4109.
34 A. B. D. Cassie, *Discuss. Faraday Soc.*, 1948, **3**, 11.
35 J. Isaelachvili and M. Gee, *Langmuir*, 1989, **5**, 288.
36 J. Hautman and M. L. Klein, *Phys. Rev. Lett.*, 1991, **67**, 1763.
37 W. Mar and M. L. Klein, *J. Phys.: Condens. Matter*, 1994, **6**, A381.
38 C. F. Fan and T. Cagin, *J. Chem. Phys.*, 1995, **103**, 9053.
39 M. Lundgren, N. L. Allen and T. Cosgrove, *Langmuir*, 2007, **23**, 1187.
40 T. Werder, J. H. Walther, R. L. Jaffe, T. Halicioglu and P. Koumoutsakos, *J. Phys. Chem. B*, 2003, **107**, 1345.
41 G. E. Poirier, *Chem. Rev.*, 1997, **97**, 1117.
42 C. Vericat, M. E. Vela, G. A. Benitez, J. A. M. Gago, X. Torrelles and R. C. Salvarezza, *J. Phys.: Condens. Matter*, 2006, **18**, R867.
43 X. Torrelles, C. Vericat, M. Vela, M. H. Fonticelli, M. Millone, R. Felici, T. Lee, J. Zegenhagen, G. Munoz, J. A. Martin-Gago and R. C. Salvarezza, *J. Phys. Chem. B*, 2006, **110**, 5586.
44 C. E. D. Chidsey and D. N. Loiacono, *Langmuir*, 1990, **6**, 682.
45 R. G. Nuzzo, E. M. Korenic and L. H. Dubois, *J. Chem. Phys.*, 1990, **93**, 767.
46 N. Camillone, C. E. D. Chidsey, G. y. Liu and G. J. Scoles, *Chem. Phys.*, 1993, **98**, 3503.
47 P. Fenter, P. Eisenberger and K. S. Liang, *Phys. Rev. Lett.*, 1993, **70**, 2447.

48 J.-P. Bucher, L. Santesson and K. Kern, *Appl. Phys. A*, 1994, **10**, 979.
49 E. Delamarche, B. Michel, C. Gerber, D. Anselmetti, H.-J. Güntherodt, H. Wolf and H. Ringsdorf, *Langmuir*, 1994, **10**, 2869.
50 G. E. Poirier and M. J. Tarlov, *Langmuir*, 1994, **10**, 2853.
51 J. Hautman and M. L. Klein, *J. Chem. Phys.*, 1989, **91**, 4994.
52 J. Hautman and M. L. Klein, *J. Chem. Phys.*, 1990, **93**, 7483.
53 W. Mar and M. L. Klein, *Langmuir*, 1994, **10**, 188.
54 M. Sprik, E. Delamarche, B. Michel, U. Rothlisberger, M. L. Klein, H. Wolf and H. Ringsdorf, *Langmuir*, 1994, **10**, 4116.
55 A. J. Pertsin and M. Grunze, *Langmuir*, 1994, **10**, 3668.
56 R. Bhatia and B. J. Garrison, *Langmuir*, 1997, **13**, 4038.
57 T. Li, I. Chao and Y. Tao, *J. Phys. Chem. B*, 1998, **102**, 2935.
58 R. Bhatia and B. J. Garrison, *Langmuir*, 1997, **13**, 765.
59 S. Vemparala, B. B. Karki, R. K. Kalia, A. Nakano and P. Vashishta, *J. Chem. Phys.*, 2004, **121**, 4323.
60 B. Rai, P. Sathish, C. P. Malhotra, Pradip and K. G. Ayappa, *Langmuir*, 2004, **20**, 3138.
61 O. Alexiadis, V. A. Harmandaris, V. G. Mavrantzas and L. Delle Site, *J. Phys. Chem. C*, 2007, **111**, 6380.
62 A. Riposan and G. Liu, *J. Phys. Chem. B*, 2006, **110**, 23926.
63 S. R. Holmes-Farley, C. D. Bain and G. M. Whitesides, *Langmuir*, 1988, **4**, 921.
64 O. Dannenberger, K. Weiss, H.-J. Himmel, B. Jager, M. Buck and C. Woll, *Thin Solid Films*, 1997, **307**, 183.
65 D. Frenkel and B. Smit, *Understanding Molecular Simulation*, Academic Press, London, 2nd edn, 2002.
66 J. C. Phillips, R. Braun, W. Wang, J. Gumbart, E. Tajkhorshid, E. Villa, C. Chipot, R. D. Skeel, L. Kale and K. Schulten, *J. Comput. Chem.*, 2005, **26**, 1781.
67 S. Miyamoto and P. A. Kollman, *J. Comput. Chem.*, 1992, **13**, 952.
68 J. P. Ryckaert, G. Ciccotti and H. J. C. Berendsen, *J. Comput. Phys.*, 1977, **23**, 327.
69 H. J. C. Berendsen, J. R. Grigera and T. P. Straatsma, *J. Phys. Chem.*, 1987, **91**, 6269.
70 W. L. Jorgensen, *J. Phys. Chem.*, 1986, **90**, 1276.
71 W. L. Jorgensen, J. D. Madura and C. J. Swenson, *J. Am. Chem. Soc.*, 1984, **106**, 6638.
72 T. A. Darden, D. M. York and L. G. Pederson, *J. Chem. Phys.*, 1993, **98**, 10089.
73 U. Essmann, L. Perera, M. L. Berkowitz, T. Darden, H. Lee and L. Pederson, *J. Chem. Phys.*, 1995, **103**, 8577.
74 M. J. de Ruijter, T. D. Blake and J. D. Coninick, *Langmuir*, 1999, **15**, 7836.
75 L. Boruvka and A. W. Neumann, *J. Chem. Phys.*, 1977, **66**, 5464.
76 A. Amirfazli and A. W. Neumann, *Adv. Colloid Interface Sci.*, 2004, **110**, 121.
77 A. Milchev and A. Milchev, *Europhys. Lett.*, 2001, **56**, 695–701.
78 A. Glättli, X. Daura and W. F. van Gunsteren, *J. Chem. Phys.*, 2002, **116**, 9811.
79 A. E. Ismail, G. S. Grest and M. J. Stevens, *J. Chem. Phys.*, 2006, **125**, 014702.
80 M. Rauscher and S. Dietrich, *Annu. Rev. Mater. Res.*, 2008, **38**, 143–172.